

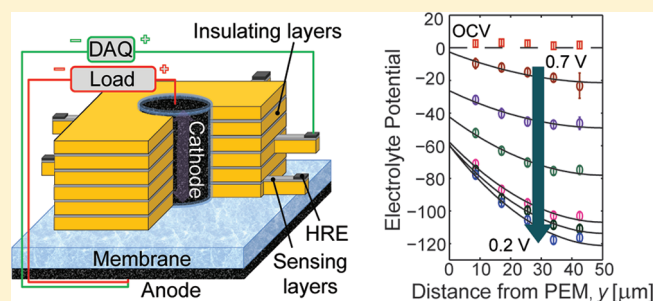
Spatially Resolved, In Situ Potential Measurements through Porous Electrodes As Applied to Fuel Cells

Katherine C. Hess, William K. Epting, and Shawn Litster*

Department of Mechanical Engineering, Carnegie Mellon University, Pittsburgh, Pennsylvania 15213, United States

ABSTRACT: We report the development and use of a microstructured electrode scaffold (MES) to make spatially resolved, in situ, electrolyte potential measurements through the thickness of a polymer electrolyte fuel cell (PEFC) electrode. This new approach uses a microfabricated apparatus to analyze the coupled transport and electrochemical phenomena in porous electrodes at the microscale. In this study, the MES allows the fuel cell to run under near-standard operating conditions, while providing electrolyte potential measurements at discrete distances through the electrode's thickness. Here we use spatial distributions of electrolyte potential to evaluate the effects of

Ohmic and mass transport resistances on the through-plane reaction distribution for various operating conditions. Additionally, we use the potential distributions to estimate the ionic conductivity of the electrode. Our results indicate the in situ conductivity is higher than typically estimated for PEFC electrodes based on bulk polymer electrolyte membrane (PEM) conductivity.



Many promising electrochemical energy conversion and storage devices (e.g., fuel cells and batteries) rely on porous electrodes to facilitate high power and energy densities. Porous electrodes provide high amounts of electrochemically active surface area compared to nonporous electrodes but also require a transport network to efficiently distribute reactants to the active surfaces. Through-plane resistances across the thickness of porous electrodes can be a major limiting factor in the performance of these devices, including PEFCs.

With their low operating temperature and high power density, PEFCs are promising energy conversion devices for efficient, low-emission transportation and portable power generation. However, there are many technological hurdles to overcome before PEFCs simultaneously meet performance, cost, and durability targets.¹ The costly platinum (Pt) catalyst used for the oxygen reduction reaction (ORR) in PEFC cathodes is underutilized due to transport limitations in the electrode. As a result of the high Pt loadings, the electrodes are the most costly component of automotive fuel cell stacks.¹

Figure 1 illustrates a PEFC electrode (often referred to as the catalyst layer) where primary aggregates of carbon supported Pt catalyst particles are bound by a Nafion ionomer film into a porous agglomerate structure.^{2–4} Between the agglomerates are larger secondary pores and within the agglomerates are smaller primary pores. Protons travel through the ionomer while electrons travel through the carbon black and Pt particles. Oxygen enters from the gas diffusion layer (GDL) and travels across the electrode's thickness through the secondary pores. It then locally dissolves into, and diffuses through, the Nafion film to meet the protons and electrons at a triple-phase boundary on a Pt particle surface.⁵ Despite being thin (<50 μm), large variations in

oxygen concentration, electrolyte potential, and reaction rates can develop across the thickness of these electrodes due to transport resistances. These resistances arise from the intrinsic resistance of the electrode materials, as well as from the fractional volume and tortuous pathways of the transport media.³ In addition, the Nafion's protonic resistance is highly sensitive to hydration and increases under dryer conditions. As a result of these resistances, regions near the GDL and the PEM are prone to becoming proton and oxygen transport limited, respectively. Thus, many experimental and modeling studies have focused on improving the materials, relative composition, and morphology of PEFC electrodes.^{4,6–10}

One limitation of many existing electrochemical diagnostic methods for porous electrodes, including those in PEFCs, is that they interface with the electrodes as either surfaces or bulk volumes and often only provide data based on cell terminal measurements. However, several techniques have been developed recently for gathering in situ measurements in the membrane electrode assembly (MEA) of a PEFC. Büchi et al.¹¹ pressed gold wires between Nafion membranes to measure the through-plane resistance distributions, while Takaichi et al.¹² used Pt wire probes placed within the membrane to measure the oxygen partial pressure. Additionally, Piela et al.¹³ studied several reference electrode (RE) placements for separating the anode and cathode potentials in an MEA.

Unfortunately, it is not feasible to investigate PEFC electrodes using the probes described above due to their large size and the

Received: August 24, 2011

Accepted: October 31, 2011

Published: October 31, 2011

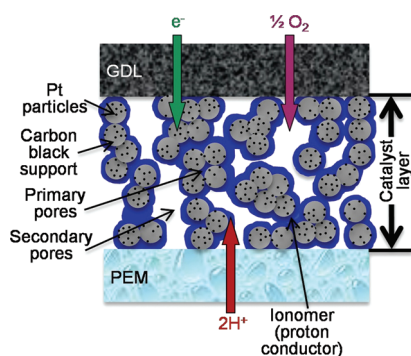


Figure 1. Schematic of a PEM fuel cell cathode. Protons from the anode cross the PEM and electrons travel through an external load. They react with oxygen at Pt catalyst particles, producing water according to the ORR. The oxygen is delivered from the gas channels through an adjacent porous carbon GDL.

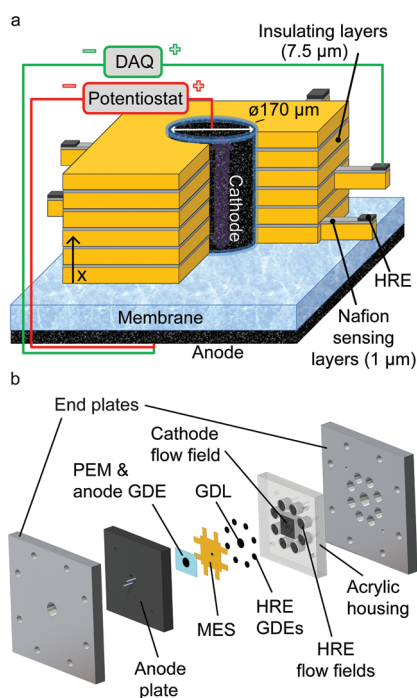


Figure 2. Schematics of the MES for electrolyte potential measurements through the thickness of a PEFC cathode (a) and the corresponding fuel cell hardware (b).

disturbance they would have on the macroscopically one-dimensional transport. To the best of our knowledge, the works by Ng et al.¹⁴ and Harris et al.¹⁵ are the only prior methods developed for direct, in situ measurements of through-plane distributions in porous electrodes during operation; both were developed for Li-ion batteries. Ng et al. used multiple planar working electrodes separated by electrolyte separator layers, each with their own current collector mesh, to measure charging rate distributions through the thickness of a Li-ion battery electrode. However, this approach yields a less representative, discontinuous electrode with insufficient resolution for PEFC electrodes. Furthermore, the electrolyte separators would prevent through-plane oxygen transport in PEFCs. Harris et al. used the change in color of graphite with lithiation to evaluate charging distributions in thick

Li-ion negative electrodes, which restricts that approach to those electrodes.

In this study, we present a new approach that uses an MES to measure electrolyte potential distributions through the thickness of a PEFC cathode. As Figure 2a shows, the MES for these measurements consists of alternating Kapton insulating layers and Nafion sensing layers that surround a column of electrode material. Other MES arrangements can be made to measure concentration, current, reaction rate, and charging distributions. Each Nafion sensing layer intersects with the electrode at a known, discrete distance through the column's thickness and protrudes out to a hydrogen reference electrode (HRE) for potential measurements. In this work, the electrolyte potential is simultaneously measured at five known locations through the electrode. Here we use the measurements to evaluate the proton transport resistance in situ as well as the distribution of the ORR across the cathode thickness under various operating conditions.

THEORY

The macroscopic one-dimensional proton transport through the electrode can be described by the conservation of current equation:

$$\frac{\partial}{\partial x} \left(\sigma_{\text{eff}} \frac{\partial \phi}{\partial x} \right) = j_{\text{ORR}} \quad (1)$$

where σ_{eff} is the effective ionic conductivity in the electrode, x is the distance through the electrode from the PEM side, ϕ is the local electrolyte potential, and j is the volumetric Faradiac ORR current density. Here we use this equation with two simplifying assumptions: (1) the reaction rate is uniform throughout the electrode; j is modeled as $j = i/L$ with i being the area-specific current density and L being the thickness of the electrode, and (2) the conductivity is uniform. We apply a fixed potential boundary condition, $\phi|_{x=0} = \phi_0$, at the membrane interface and a zero current boundary condition, $\partial\phi/\partial x|_{x=L} = 0$, at the GDL. With those assumptions and boundary conditions, eq 1 simplifies to

$$\phi = \frac{i}{\sigma_{\text{eff}}} \left(\frac{x^2}{2L} - x \right) + \phi_0 \quad (2)$$

where ϕ_0 is the potential at the interface of the electrode with the PEM. We later use this solution to evaluate the measured potential distributions relative to a uniform distribution. In addition, ϕ_0 and σ_{eff} can be estimated by fitting MES data to eq 2 using these two variables as fitting parameters.

EXPERIMENTAL SECTION

We fabricated the MES by spin coating a $\sim 1 \mu\text{m}$ thick layer of Nafion from a 15 wt % Nafion solution (Ion Power, New Castle, DE) onto a 7.5 μm thick sheet of Kapton (American Duraform, Holliston, MA). Once dry, a laser engraver (Pinnacle, V-series) cut the bilayers to the desired shape: a square with a protruding tab on one edge. They were then stacked such that none of the protruding tabs overlapped, and a square of uncoated Kapton was placed on top, insulating the exposed Nafion layer. The resulting 50 μm thick stack was hot pressed at 2.8 MPa and 125 °C for 4 min. A 170 μm diameter hole was then laser micromilled (New Wave, Fremont, CA) into the center of the stack. We chose this diameter because it is small enough that

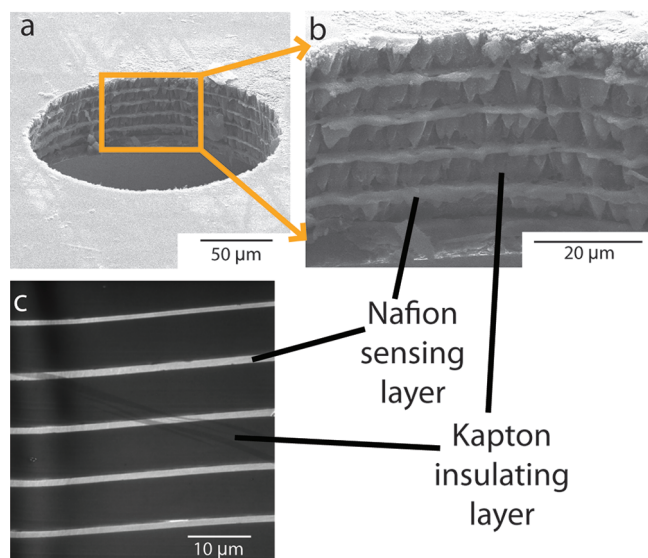


Figure 3. Electron micrographs of MES substrates. (a) SEM image of a laser-cut hole in the MES, (b) SEM image showing alternating Nafion (light) and Kapton (dark) layers inside of the hole, and (c) TEM image of alternating Nafion and Kapton layers showing approximately uniform $1\ \mu\text{m}$ thick sensing layers.

transport through the electrode can be considered nearly one-dimensional, but large enough to permit hand painting of the catalyst ink. A scanning electron microscope (SEM) image of an MES with a $200\ \mu\text{m}$ diameter hole is shown in Figure 3a with a close up of the laser cut layers shown in Figure 3b. In addition, Figure 3c shows a transmission electron microscope (TEM) image of an ultramicrotome slice of the MES substrate cross-section with nearly uniform, $\sim 1\ \mu\text{m}$ thick Nafion sensing layers.

A catalyst ink suspension was made by combining Pt/C catalyst (20% Pt/C on Vulcan XC-72R, HiSPEC 3000, Alfa-Aesar, Ward Hill, MA), 5 wt % Nafion solution (DE-521, Ion Power), and a small amount of deionized water for a final Nafion loading of 33% wt. The mixture was placed in an ultrasonication bath for 5 min and then mixed overnight on a magnetic stirrer. To assemble the MES, a Nafion 115 membrane (Ion Power) and then a $0.4\ \text{cm}^2$ commercial gas diffusion electrode (GDE) (Electrochem EC-20-10-7 Electrode, Woburn, MA) impregnated with Nafion solution were adhered to the bottom of the MES stack by hot pressing at $125\ ^\circ\text{C}$ for 4 min at $0.71\ \text{MPa}$ and $70\ \text{kPa}$, respectively. Once the assembly was bonded, the catalyst ink was painted into the hole in the MES with the aid of a stereoscopic microscope and then dried at room temperature. The painting process was repeated until the hole was filled to the height of the MES. Finally, a $0.4\ \text{cm}^2$ conventional GDL (SGL-24BC, Ion Power) was hot pressed to the top of the MES.

Specialized fuel cell hardware, shown in Figure 2b, was designed and fabricated for MES diagnostics. The hardware resembles that for a traditional PEFC with serpentine channels milled into graphite plates for the anode and cathode flow fields. However, the cathode plate is embedded in an acrylic chassis, which additionally houses up to eight electrically isolated HRE flow fields for separately delivering air to the cathode and hydrogen to the HREs. Each HRE is sealed with an O-ring to prevent gas leakage. Thus, the only gas transport pathway is through the long, thin Nafion sensing layers, which present a much higher transport resistance than the normal hydrogen and

oxygen crossover through the membrane. Two tubulations (Scanivalve, Liberty Lake, WA) protrude from the back of each flow field to provide gas delivery. One additional tubulation is attached to each flow field with conductive silver epoxy (EPO-TEK, Billerica, MA) for measuring the cell's current and potential and the HRE potentials.

In addition to the MES assembly, a conventional $1\ \text{cm}^2$ MEA was prepared for verifying that the MES cathode was representative of a normal electrode. The $1\ \text{cm}^2$ MEA was prepared from the same batch of catalyst ink and the same Nafion impregnated GDE as the MES to eliminate variability between materials. The ink was hand painted onto a Nafion 115 membrane with a target loading of $0.7\ \text{mg}_{\text{Pt}}/\text{cm}^2$, which was chosen to roughly match the $50\ \mu\text{m}$ thickness of the MES cathode.

A fuel cell test stand (850e, Scribner and Associates, Southern Pines, NC) controlled the fuel cell temperature and supplied air to the cathode and H_2 to the anode with the desired dew point temperatures and flow rates. Air and H_2 flow rates of 0.2 and 0.3 slpm, respectively, were used and result in very high stoichiometric ratios given the small area of the MES cathode. The same constant flow rates were used for the $1\ \text{cm}^2$ MEA resulting in stoichiometric ratios of 12 and 29, at a current density of $1\ \text{A}/\text{cm}^2$, for the air and H_2 , respectively. During ionic potential measurements, the HREs were held under the same temperature and humidity conditions as the anode at all times. A potentiostat (VSP, Biologic, Knoxville, TN) controlled the fuel cell voltage, measured the current, and performed electrochemical impedance spectroscopy (EIS). A data acquisition board (DAQ) (National Instruments, Austin, TX) simultaneously collected potential data versus the cathode from the HREs and the anode. All experiments used a Faraday cage (Technical Manufacturing Corporation, Peabody, MA) and shielded cables to minimize noise.

N_2/H_2 cyclic voltammetry (CV) measurements were performed with fully humidified gases at a cell temperature of $30\ ^\circ\text{C}$ with a scan rate of $40\ \text{mV}/\text{s}$ between potentials of 0 and $0.8\ \text{V}$. Electrochemically active surface area measurements were based on the CV's current–voltage curve area for hydrogen desorption, correcting for the electric double layer charging current. For potentiostatic polarization curves, potentials greater than $0.8\ \text{V}$ were held for 60 s, while lower potentials were held for 10 min. The data presented are time-averages of the current and MES potential data for the last 30 and 90 s of the voltage holds for potentials $>0.8\ \text{V}$ and $\leq 0.8\ \text{V}$, respectively. At the end of each potential hold, EIS was performed over a frequency range of 0.1 Hz to 300 kHz to obtain the high frequency resistances and generate IR-free polarization curves. Throughout the experiment, fully humidified hydrogen was delivered to HREs being held at the fuel cell temperature. Before performing experiments, we assured the continuity of the Nafion films by measuring the current when $0.5\ \text{V}$ was applied between any two of the HREs. All HREs used here provided a current of $1\ \mu\text{A}$ or greater, with an average value of $5.2\ \mu\text{A}$ and a standard deviation of $1.7\ \mu\text{A}$, which indicated that the sensing layers were in good contact with the electrode's Nafion phase.

RESULTS AND DISCUSSION

Comparison of the MES Assembly with a $1\ \text{cm}^2$ MEA. We first present a comparison of the MES assembly with a $1\ \text{cm}^2$ MEA to verify that the cathode in the MES adequately replicates the characteristics of that in a conventional fuel cell. We note that

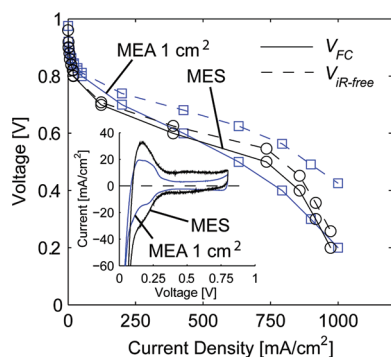


Figure 4. Comparison between the electrochemical characteristics of an MES and a 1 cm² MEA. The solid lines in the main plot are the polarization data collected at 57/57/35 °C (anode dew point/cell/cathode dew point); dashed lines show the IR-free curves. The inset shows cyclic voltammograms measured for the MES and the 1 cm² MEA with the vertical axis being the area-specific current density.

a post-mortem SEM of the 1 cm² MEA showed a cathode thickness closer to 40 μm rather than the 50 μm of the MES, entailing a somewhat lower Pt loading. This reduced thickness was also evidenced by a reduced area in the hydrogen desorption portion of the 1 cm² MEA's CV plot (Figure 4 inset), which is proportional to the electrochemical surface area (ECSA). Looking at the inset we see that the CVs have different profiles, which has been shown to arise from high N₂ gas flow rates and the increased removal of evolved hydrogen from the working electrode.^{16,17} This effect is consistent with extremely high N₂ flow rates (0.2 slpm) relative to the very small MES cathode.

The mass specific ECSA values calculated from the MES and 1 cm² MEA CV curves in Figure 4 compare reasonably well when accounting for the ink composition, material densities, thicknesses, and estimated porosity of 50%. We obtain ECSA values of 56 m²_{Pt}/g_{Pt} for the MES cathode and 45 m²_{Pt}/g_{Pt} for the 1 cm² MEA cathode. These values are within the expected range for this catalyst,¹⁸ suggesting the MES hole was successfully filled with catalyst ink. We additionally observe roughly 7 times greater hydrogen crossover current density in the MES cathode's CV compared to the 1 cm² MEA. This is identified by the positive shift of the EDL charging current as well as a lower OCV of 0.96 V for the MES compared to 0.98 V for the 1 cm² MEA. We presume this is due to the large ratio of the anode to cathode area in the MES. This area asymmetry manifests itself as increased effective transport area through the membrane that reduces the resistances for water and hydrogen diffusion and proton conduction.

Figure 4 presents potentiostatic polarization curves for both the MES and the 1 cm² MEA at 57/57/35 °C (anode dew point/cell/cathode dew point). These curves show reasonable agreement over the entire voltage range, but have some notable differences. There is an apparent lack of activity in the MES at potentials around 0.8 V. In addition, there was a noticeable transient decrease in current with the MES during the first extended potential hold at 0.8 V, consistent with changes in the Pt oxide coverage conditions.¹⁹ These differences at high potentials could be due to higher rates of hydrogen crossover or anode to cathode water diffusion. It is also possible that the isolated, microscale MES cathode exhibits oxide coverage effects more clearly than full-scale cathodes.

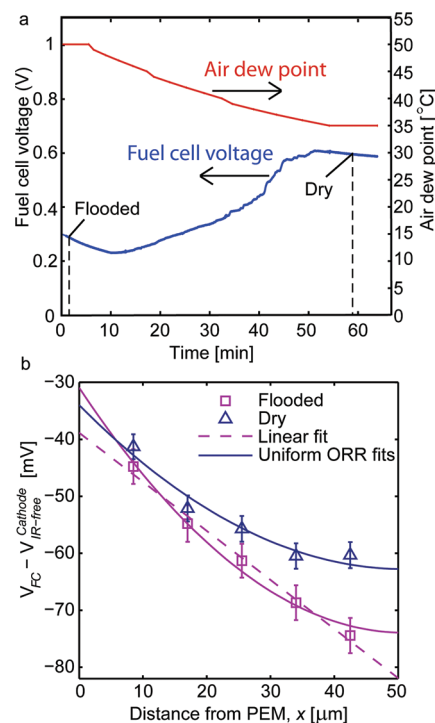


Figure 5. Effects of flooding and drying on the potential distribution through the electrode. (a) Voltage and temperature time-series as the cathode dew point changed from 50 to 35 °C during a galvanostatic hold at 520 mA/cm². (b) Electrolyte potential distributions for both flooded (57/57/50 °C) and dry (57/57/35 °C) times indicated by the dashed lines in part a. Potential data for each case was averaged over 60 s. Error bars are an rms combination of the HRE standard deviation at OCV (2 mV) and the temporal variations of each HRE over the time-averaging period.

Comparing the IR-free polarization curves, we first note the Ohmic resistances are 4 times higher for the 1 cm² MEA than the MES, probably because of the MES electrode asymmetry. Examining the IR-free curves further, we observe the MES and 1 cm² MEA have very similar IR-free potentials at roughly 750 mA/cm² and both begin to exhibit increasing mass transport limitations at currents above this value. The higher IR-free potential of the 1 cm² MEA at higher currents is most likely because of reduced flooding in the slightly thinner cathode. Indeed, the MES exhibited more severe flooding than the 1 cm² MEA when the air dew point was increased.

From the preceding analysis, we conclude that MES diagnostics fall in between the techniques of rotating disk electrode (RDE) and single cell MEA diagnostics. It allows for analysis of transport in an electrode under representative operating conditions, unlike RDE. However, because of the reduced membrane transport resistances arising from electrode area asymmetry, exact MEA conditions cannot be identically recreated. A possible way to minimize this discrepancy when applying MES diagnostics in the future is to match membrane transport resistances by using thicker membranes than those in the anticipated PEFC.

Transient Changes in Potential Distribution. Here we present results from an experiment during which the fuel cell was held at a current of 520 mA/cm² and temperature of 57 °C, while the air dew point was changed from 50 to 35 °C. During this experiment, the MES measured the electrolyte potential distribution across the cathode's thickness. Figure 5a presents the

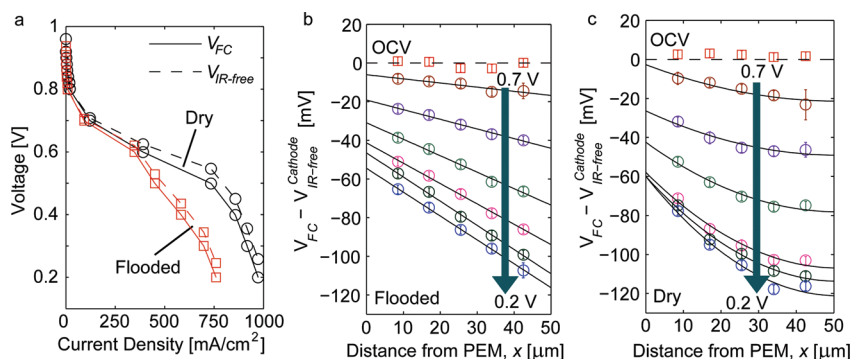


Figure 6. Polarization curves and electrolyte potential distributions through the thickness of the electrode as measured by the MES. (a) Polarization and IR-free curves for both flooded (57/57/50 °C) and dry (57/57/35 °C) conditions. (b) Electrolyte potential distributions through the thickness of the MES in flooded conditions during potentiostatic holds; starting with OCV (\square) then 0.7 to 0.2 V (\circ). The solid lines are linear fits at each fuel cell potential. (c) Electrolyte potential distributions through the thickness of the MES in dry conditions during potentiostatic holds; starting with OCV (\square) then 0.7 to 0.2 V (\circ). Solid lines show the analytical solution for a uniform reaction rate at each fuel cell potential.

Table 1. Fitting Parameters for Potential Distribution under Dry Conditions Shown in Figure 6c, Including the Measured Ohmic Overpotential, η_{ohm}

V_{FC} [V]	η_{ohm} [mV]	ϕ_o [mV]	σ [S/m]	R^2	% Err $ \eta_{\text{ohm}} + \phi_o / \eta_{\text{ohm}}$
0.6	25.1	-26.4	4.40	0.923	5.18
0.5	46.2	-42.4	5.44	0.974	8.23
0.4	51.1	-57.9	4.45	0.980	13.3
0.3	56.3	-59.9	4.34	0.987	6.39
0.2	57.9	-60.0	4.05	0.979	3.63

air dew point and fuel cell voltage time-series over roughly a 1 h portion of the experiment. At early times, the fuel cell exhibited a low, decreasing voltage due to electrode flooding. As the air's dew point cooled to 35 °C, we observed a corresponding increase in voltage, indicating the evaporation of accumulated liquid water. After the dew point reached 35 °C, we observed a small initial decrease in fuel cell voltage consistent with the initial drying of Nafion and increasing Ohmic losses.

Figure 5b plots the through-plane electrolyte potential distributions across the cathode at the times indicated in Figure 5a and with the data points being a time-average value over a 60 s period. The error bars are the rms combination of the standard deviation of the HREs at OCV and the temporal variations of each HRE during the averaging period. This led to error bars in the range of 2–4 mV. First, we observe in both cases that the potential gradient for the first two points and their extrapolated intercepts with the y-axis are nearly identical. Given the constant current density, this indicates negligible change in the proton conductivity in the membrane and in the portion of the electrode near the PEM. This is expected since the dry condition data was gathered at the beginning of the transient drying process. The key difference between the two profiles is the significant flattening of the dry profile near the GDL, whereas the flooded profile is roughly linear throughout as illustrated by the R^2 value of 0.99 for the linear fit shown. Figure 5b also includes fits to the two profiles for a uniform, one-dimensional ORR distribution from eq 2 for a volumetric ORR rate of 104 A/cm³ consistent with the 520 mA/cm² current density. The linear profile of the flooded case indicates that the ORR is concentrated near the GDL interface due to mass transport limitations within the electrode. In other words, since the potential gradient is uniform up to the last

measurement point, the current is also uniform. This means the proton current is primarily being consumed between the last sensing layer and the GDL. In contrast, the notable flattening of the dry distribution near the GDL suggests that the electrode is relatively more proton transport limited due to Ohmic losses and the reaction has shifted toward the PEM interface. From the data in Figure 5b, we can also estimate the electrode's ionic conductivity using Ohm's law with the ~ 10 mV potential drop between the first two data points, their 8.5 μm spacing, and the 520 mA/cm² current density. This leads to an effective conductivity of 4.5 S/m.

Polarization Curve Analysis. We performed polarization curve experiments to elucidate the effects of fuel cell potential and current density on the electrolyte potential distributions under high and low humidity conditions. The potentiostatic polarization curves were measured from open circuit voltage (OCV) to 0.2 V at a cell temperature of 57 °C with fully humidified hydrogen. The air dew point temperatures for the high and low humidity conditions were 50 and 35 °C, respectively. The corresponding polarization curves in Figure 6a show greater mass transport losses and lower limiting current densities in the high humidity condition due to liquid water flooding. However, the Ohmic losses did not seem to vary significantly between the two cases because the fully humidified hydrogen and small MES area act to maintain membrane hydration in both cases.

Figure 6b,c shows how the electrolyte potential distributions change through the thickness of the electrode under two different humidity conditions and for fuel cell potentials ranging from 0.7 to 0.2 V in 0.1 V increments. In Figure 6b, we have plotted linear fits to the high humidity condition as this has proven to be the better fit for a flooded electrode. The linear trend at the highest potentials for the flooded conditions suggests that the cell is mass transport limited even at low currents. Flooding at low currents is possibly due to the high anode humidity and the MES electrode asymmetry that increases the relative water diffusion rates from anode to cathode. Our analysis shows that as the current increases, the linear fit improves from an R^2 value of 0.898 to 0.999. This is expected: more water is produced at higher currents, impeding oxygen transport and driving the reaction toward the GDL even further.

The dry case, shown in Figure 6c, appears to match the analytical solution for uniform ORR well at most currents. This implies that even at high currents, the cell does not become as severely mass transport limited. In fact, the flattening out of the two data points farthest from the membrane indicates that the cell is somewhat proton transport limited and that more of the reaction is occurring closer to the PEM. However, at the highest currents it is apparent that the profile becomes more linear toward the PEM side, which is consistent with the fuel cell being in the mass transport limited portion of the polarization curve.

We now analyze the fits to the distributions to extract information regarding the effective ionic conductivity and the through-plane uniformity of the ORR. Table 1 lists the fit values for ϕ_o and σ_{eff} , along with the Ohmic potential drop, η_{ohm} , measured by EIS for the dry condition data in Figure 6c. The values for the 0.7 V hold are not shown because of the large, unsystematic variability associated with the point nearest the GDL that was likely due to a water droplet entering the HRE during the time-averaging. We note that there is generally less than a 10% difference between the ϕ_o and η_{ohm} values, indicating that the value of the high frequency resistance is primarily due to the PEM's resistance. This good agreement for the PEM's potential drop, and the high R^2 values suggest that the fits to the data are both reasonably precise and accurate. We conclude that the conductivity values calculated from the fits and listed in Table 1 are representative estimations, typically ranging between 4.0 and 4.5 S/m.

The conductivity values from the fits as well as those estimated from the initial slopes in Figure 5b, agree well with the recent measurements taken by Liu et al.²⁰ for the same ionomer/carbon (Vulcan XC-72R) weight ratio of 0.6 and oversaturated gases. Using EIS analysis on an N_2/H_2 cell, they found the resistivity to be $\sim 25 \Omega \text{ cm}$ in their work, which translates to $\sim 4 \text{ S/m}$. Although our measurements of $\sim 4.5 \text{ S/m}$ ($\sim 22 \Omega \text{ cm}$) agree well with Liu et al.'s results, we find that these conductivities are higher than our anticipated value of less than 1 S/m. We estimated this value using the bulk conductivity of Nafion equilibrated with liquid water at 330 K (13 S/m),²¹ a realistic tortuosity of roughly 3, and an expected Nafion volume fraction of 0.2, where the Nafion volume fraction is estimated based on the Nafion loading, density of Nafion, and the electrode thickness.²⁰ These high conductivities led Liu et al. to estimate nonphysical tortuosity factor values as low as 0.5 when considering their estimates of Nafion volume fraction and their measured values for the conductivity of cast Nafion films. Because tortuosity values below unity are not physical, this suggests an unknown mechanism causing abnormally high conductivity in the electrode.

We suggest three possible causes for the high conductivity given ex situ studies have shown that thin Nafion films exhibit lower conductivity than bulk.²² (1) Water generation within the agglomerates results in nonequilibrium water content levels (above an $\text{H}_2\text{O}/\text{SO}_3^-$ ratio of 22 for liquid water equilibrated Nafion²¹) due to water desorption resistances and increases the conductivity within the electrode. (2) Water films surrounding the Nafion provide proton transport bridges that reduce tortuosity and increase local mobility. Because of the porosity and pore morphology of Nafion, protons have roughly 5 times higher mobility in water.^{21,23} (3) Surface conduction mechanisms and acidic groups on the carbon catalyst support may increase the electrode's conductivity. Thus, additional research is required

to elucidate the proton conduction mechanisms in PEFC electrodes.

CONCLUSIONS

MES diagnostics are a novel approach for gathering in situ, through-plane measurements within a porous electrode. Here we used an MES to gather electrolyte potential data at five points through the thickness of the cathode in a PEFC running at near-standard fuel cell operating conditions. This data allowed us to study, in situ, the reaction rate distribution and the state of flooding in the electrode during flooded and dry conditions for the first time. Additionally, we were able to calculate a higher than expected ionic conductivity value of $\sim 4.5 \text{ S/m}$, which matched well with results from a recent study using EIS on an N_2/H_2 cell.

AUTHOR INFORMATION

Corresponding Author

*E-mail: litster@andrew.cmu.edu.

ACKNOWLEDGMENT

The authors gratefully acknowledge the support of a National Science Foundation (NSF) Faculty Early Career Development (CAREER) award for S. Litster as well as a U.S. Environmental Protection Agency (EPA) STAR Fellowship to W. K. Epting.

REFERENCES

- (1) Papageorgopoulos, D. *Proc. DOE Hydrogen Program Annual Merit Review*, Washington, DC, May 10 2011.
- (2) Harvey, D.; Pharoah, J. G.; Karan, K. *J. Power Sources* **2008**, *179*, 209–219.
- (3) Litster, S.; McLean, G. *J. Power Sources* **2004**, *130*, 61–76.
- (4) Uchida, M.; Aoyama, Y.; Eda, N.; Ohta, A. *J. Electrochem. Soc.* **1995**, *142*, 4143–4149.
- (5) O'Hayre, R.; Barnett, D. M.; Prinz, F. B. *J. Electrochem. Soc.* **2005**, *152*, A439–A444.
- (6) Eikerling, M.; Kornyshev, A. A. *J. Electroanal. Chem.* **1998**, *453*, 89–106.
- (7) Marr, C.; Li, X. *J. Power Sources* **1999**, *77*, 17–27.
- (8) Sun, W.; Peppley, B. A.; Karan, K. *Electrochim. Acta* **2005**, *50*, 3359–3374.
- (9) Wilson, M. S.; Gottesfeld, S. *J. Appl. Electrochem.* **1992**, *22*, 1–7.
- (10) Springer, T. E.; Zawodzinski, T. A.; Gottesfeld, S. *J. Electrochem. Soc.* **1991**, *138*, 2334–2342.
- (11) Büchi, F. N.; Scherer, G. G. *J. Electrochem. Soc.* **2001**, *148*, A183–A188.
- (12) Takaichi, S.; Uchida, H.; Watanabe, M. *Electrochim. Acta* **2008**, *53*, 4699–4705.
- (13) Piela, P.; Springer, T. E.; Davey, J.; Zelenay, P. *J. Phys. Chem. C* **2007**, *111*, 6512–6523.
- (14) Ng, S.-H.; La Mantia, F.; Novák, P. *Angew. Chem., Int. Ed.* **2009**, *48*, 528–532.
- (15) Harris, S. J.; Timmons, A.; Baker, D. R.; Monroe, C. *Chem. Phys. Lett.* **2010**, *485*, 265–274.
- (16) Lindstrom, R. W.; Kortsdottir, K.; Wesselmark, M.; Oyarce, A.; Lagergren, C.; Lindbergh, G. *J. Electrochem. Soc.* **2010**, *157*, B1795–B1801.
- (17) Schneider, I. A.; Kramer, D.; Wokaun, A.; Scherer, G. G. *Electrochem. Commun.* **2007**, *9*, 1607–1612.
- (18) <http://www.jmfuelcells.com/fccatalysts.html>, 2011.
- (19) Parthasarathy, A.; Srinivasan, S.; Appleby, A. J.; Martin, C. R. *J. Electroanal. Chem.* **1992**, *339*, 101–121.

- (20) Liu, Y.; Ji, C.; Gu, W.; Jorne, J.; Gasteiger, H. A. *J. Electrochem. Soc.* **2011**, *158*, B614–B621.
- (21) Zawodzinski, T. A.; Derouin, C.; Radzinski, S.; Sherman, R. J.; Smith, V. T.; Springer, T. E.; Gottesfeld, S. *J. Electrochem. Soc.* **1993**, *140*, 1041–1047.
- (22) Paul, D. K.; Fraser, A.; Karan, K. *Electrochem. Commun.* **2011**, *13*, 774–777.
- (23) Lide, D. R., Ed. *CRC Handbook of Chemistry and Physics*, 87th ed.; Taylor and Francis: Boca Raton, FL, 2007; Internet Version.